Observation of Femtosecond Molecular Dynamics via Pump-Probe Gas Phase X-ray Scattering

IOP Publishing Journal of Physics B: Atomic, Molecular and Optical Physics
J. Phys. B: At. Mol. Opt. Phys. **49** (2016) 034001 (11pp) doi:10.1088/0953-4075/49/3/034001

Observation of femtosecond molecular dynamics via pump–probe gas phase x-ray scattering

J M Budarz[1,2], M P Minitti[2], D V Cofer-Shabica[1], B Stankus[1], A Kirrander[3], J B Hastings[2] and P M Weber[1]

[1] Department of Chemistry, Brown University, Providence, RI 02912, USA
[2] SLAC National Accelerator Laboratory, Menlo Park, CA 94025, USA
[3] School of Chemistry, University of Edinburgh, Edinburgh EH9 3JJ, UK

E-mail: peter_weber@brown.edu

Received 6 October 2015, revised 2 November 2015
Accepted for publication 10 November 2015
Published 8 January 2016

Abstract

We describe a gas-phase x-ray scattering experiment capable of capturing molecular motions with atomic spatial resolution and femtosecond time resolution. X-ray free electron lasers can deliver intense x-ray pulses of ultrashort duration, making them suitable to study ultrafast chemical reaction dynamics in an ultraviolet pump, x-ray probe scheme. A cell diffractometer balances sample flow with gas density and laser focusing conditions to provide adequate scattering vector resolution with high signal intensity and near-uniform excitation probability. Images from a pixel-array x-ray detector, spatially and electronically calibrated, allow for detection of scattering intensity changes below 1%. First experiments on the ring-opening reaction of 1,3-cyclohexadiene to form 1, 3, 5-hexatriene show a rapid initial reaction on an 80 fs time scale.

Keywords: femtosecond, x-ray scattering, x-ray free electron lasers, molecular dynamics

(Some figures may appear in colour only in the online journal)

1. Introduction

The study of molecules as they interact and transform, a dominant quest of chemistry for over a century, has led to a profound understanding of the nature of chemical reactions and to advanced tools used to create molecules for a myriad of applications [1–3]. Chemical reactions are accompanied by changes in molecular structure that pose experimental challenges related to the scale of the processes: atomic motions occur on the order of femtoseconds and over distances measured in ångströms.

To date, most time-resolved studies of chemical reaction dynamics employ spectroscopic techniques. In probing the energies and populations of excited states, common methods are able to follow the flow of energy through molecular systems [4–9]. Yet with few exceptions [10–14], they remain incapable of determining molecular structures. Scattering techniques, which are widely used to probe chemical structures in static systems, can be extended to perform on ultrafast timescales as well, thereby connecting spectroscopic information describing the energy flow within molecules to a structural description of the nuclear motions.

Electron scattering, the most commonly employed method for gaseous systems, has recently been extended to the ultrafast time regime with great success [15–21]. The short wavelength of electrons offers superior spatial resolution in the real space of molecular structure. Challenges to the time resolution stem from the velocity difference of the electrons compared to the excitation laser pulse that initiates the reaction in a pump–probe experiment, the mutual space-charge repulsion of electrons within a single bunch, and the timing jitter from the initial electron speeds near the cathode. Creative solutions to these issues have been advanced: relativistic electrons approach the speed of light, so that the velocity spread might not limit the time resolution [22]; recognizing that space-charge broadened pulses have almost

perfect chirp, they can be compressed [21, 23]; or, minimizing the number of electrons per pulse can avoid space-charge broadening in the first place [24]. Taking advantage of these advances, compressed electron pulses have been used to investigate the ultrafast dynamics of gold [25], to investigate the molecular dynamics of diarylethene [26], and to produce single-shot scattering patterns of aluminum [20] and gold foils [21]. For gaseous samples, while promising early studies illustrate the potential of the technique [27, 28], progress has been hampered by the small sample densities, the unfavorable scaling of scattering signals at large angles and the extended sizes of interaction regions required to reach adequate signal levels.

In the gas phase, the internal dynamics of molecular motions can be isolated as reactions proceed without the interference of nearby molecules. Therefore, gas-phase molecular dynamics are an important source of reference data and fundamental studies that compare experiments to detailed theoretical calculations. The advent of x-ray free electron lasers (XFELs) that deliver ultrashort x-ray pulses synchronized to pulsed lasers [29] presents an opportunity to observe scattering patterns even for low density gases of small organic molecules. By sidestepping many of the challenges posed by electron scattering, ultrafast x-ray scattering can examine the chemical reaction dynamics of isolated molecules.

The total elastic scattering cross-section for 1,3-cyclohexadiene, a well-known model system for chemical dynamics studies, is 7.8×10^{-24} cm^2 [30] for 20 keV x-rays. Depending on the scattering vector, this is about a factor of 10^5 smaller than comparable electron scattering cross-sections. To make up for the small cross sections, it is necessary to use an x-ray source with a very high photon flux. This is now possible through the advent of fourth generation XFELs: the linac coherent light source (LCLS) is capable of generating tunable x-rays with pulse lengths down to 2 fs and up to 10^{12} photons per pulse [31]. LCLS already has enabled novel structural studies with single x-ray pulses on macromolecules such as mimivirus particles [32] and proteins [33–35], which require a high photon flux to image structures before they are destroyed, as well as ultrafast temporal studies of nucleobase thymine via Auger spectroscopy [36].

X-ray elastic scattering maps molecular structure in amorphous (non-crystalline) samples by measuring the atom–atom pair distributions. As x-rays pass through matter some of them scatter, resulting in a momentum transfer q that is related to the scattering angle 2θ as $q = \frac{4\pi \sin\theta}{\lambda}$, where λ is the x-ray wavelength. In the independent-atom model, the rotationally averaged elastic scattering is defined as the sum of atomic and molecular contributions [37]

$$\frac{I(q)}{I_0} = \sum_{i}^{N_{\text{atom}}} \left|f_i(q)\right|^2 + \sum_{i\neq j}^{N_{\text{atom}}} f_i(q) f_j(q) \frac{\sin qr_{ij}}{qr_{ij}} \qquad (1)$$

with well-known elastic scattering atomic form factors $f_i(q)$ [38]. Here, the r_{ij} are the inter-nuclear distances and I_0 is the intensity of the incident x-ray. For molecular samples deliberately aligned or preferentially selected by a polarized excitation laser, the scattering signals additionally depend on the relative orientations of the detection vector and the laser geometry [39, 40]. The time-evolving structures of molecules undergoing a chemical reaction can be followed by measuring the scattering pattern as a function of delay time between an excitation pulse and the x-ray probe pulse. In 1,3-cyclohexadiene, the concept of a well-defined structure throughout the ring-opening is justified, since the molecule travels ballistically down the excited state surfaces [41, 42], a point to which we will return later.

The necessity of balancing opposing demands, in particular a high signal-to-noise ratio and an absence of spurious background signals, required the development of a novel diffractometer and associated experimental protocol. We present here the design of such an apparatus and discuss the methods critical to the calibration and analysis needed to produce ultrafast molecular movies using x-rays. The apparatus was successfully implemented to study the time-resolved ring-opening reaction of 1,3-cyclohexadiene [43, 44], a system for which detailed insights from the scattering experiments are discussed.

2. Methods

2.1. The pump–probe scheme

To measure time-evolving molecular structures, a pump–probe scheme is used where a laser pulse initiates the reaction and a variably delayed x-ray probe pulse maps the molecular structure at different delay times. Assuming that the optical excitation leads to deterministic dynamics, a movie is created by collaging the individual structural snapshots.

In our experimental implementation, we paired an ultraviolet excitation pulse (267 nm, 65 fs, 100 μm FWHM focus) with a variably timed x-ray probe pulse, each operating at 120 Hz. The pulses are coupled together 18 cm upstream through a mirror oriented at 45° such that they arrive at the sample region collinearly (figure 1). Scattering patterns were taken with both fundamental (8.3 keV, 0.1494 nm, 30 fs, 10^{12} photons/pulse, 30 μm FWHM focus) and 3ω (20.1 keV, 0.0617 nm, 30 fs, 10^{10} photons/pulse, 30 μm FWHM focus) wavelengths of the LCLS x-ray source. For a diffractometer with fixed angular limits, the higher-energy 3ω x-ray photon provides a larger range in q-space, but at the cost of 100 times fewer photons per x-ray pulse.

2.1.1. Determination of temporal overlap. While the exact time zero is determined as part of the data analysis, an experimental measurement of time zero is important so that data is acquired in the proper time range. With the chemical reactions of interest often proceeding within less than 1 ps (10^{-12} s), it is imperative that the proper time window is set before conducting an experiment.

At the LCLS XPP hutch [29, 45], where these experiments were carried out, coarse timing between the laser and x-rays was achieved by inserting an metal–semiconductor–metal (MSM) diode downstream of the interaction region. These diodes have a fast time response

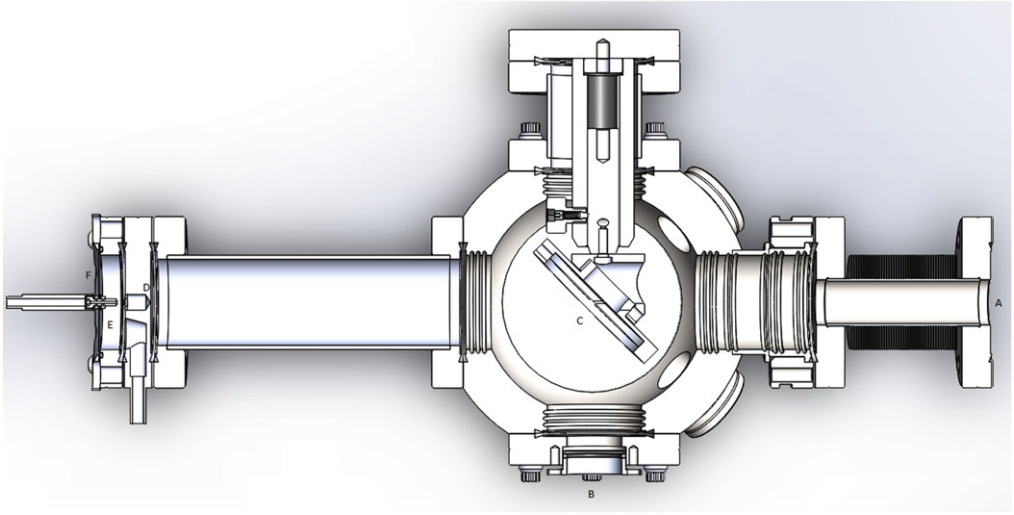

Figure 1. Cross-section of the diffractometer and vacuum chamber. The x-ray pluses are coupled into the vacuum chamber from (A), while the UV enters perpendicularly from (B). Both are superimposed through a mirror with a 500 μm hole (C) located about 18 cm upstream from the scattering cell (D).

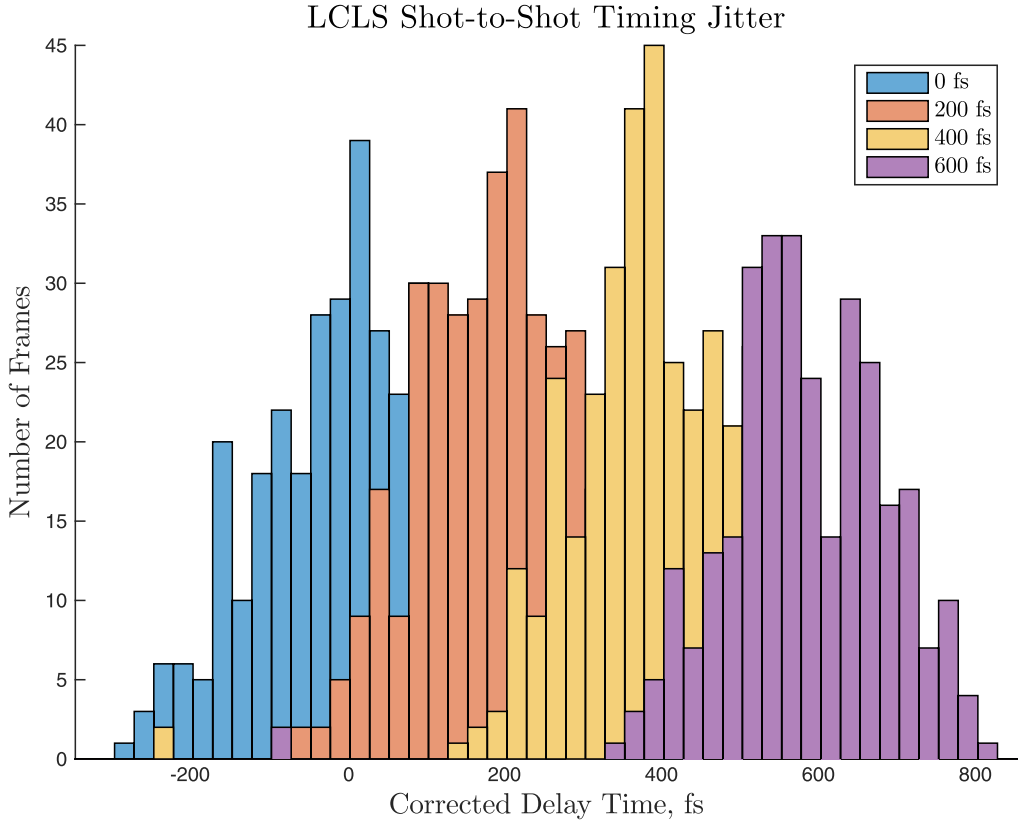

Figure 2. Experimental distribution of x-ray arrival times. Nominal time points shown are 0, 200, 400, and 600 fs.

for both the x-rays and ultraviolet laser pulses. Waveforms from the detector were measured on a remotely controlled 18 GHz oscilloscope, thus allowing coarse temporal overlap at the 10 ps level. More precise timing (<250 fs) was found using a bismuth (1, 1, 1) crystal inserted near the interaction point [46]. A similar MSM diode, positioned at the Bragg condition of bismuth at 8.3 keV (or 20.1 keV), was used to monitor the reflection of the optical laser off the bismuth target. As the relative time delay, $\Delta t = t_{\mathrm{X-ray}} - t_{\mathrm{UV}}$, crossed from positive to negative, the optical reflection of the bismuth is altered, revealing the machine-limited jitter of the temporal overlap at the interaction region in our scattering cell.

2.1.2. Jitter correction. The timing of the x-ray and optical lasers at LCLS is RF-controlled [47], but due to electrical noise there is an unpredictable shot-to-shot jitter of >250 fs

FWHM (figure 2). For experiments where femtosecond time resolution is important, this may be longer than the dynamics of interest. To determine the relative arrival times of the UV and x-ray photon pulses more accurately, a spectral encoding time-tool was employed that reduces this uncertainty to less than about 10 fs [48]. Operating on a fraction of optical laser light picked off by a beamsplitter upstream from the diffractometer, white light continuum (WLC) is generated in a sapphire substrate. The WLC is spectrally chirped and transmitted through a thin film of silicon nitride (Si_3N_4). When the film absorbs the arriving x-ray photon, the material undergoes an index of refraction change for the optical pulse, creating a change in the transmitted spectrum and a clear measure of the relative arrival of the optical and x-ray pulses. In this way, the time-delay for each collected frame of scattering pattern can be corrected, allowing images to be sorted into time-bins as small as 25 fs.

2.2. The diffractometer

High demands are placed on the design and construction of the diffractometer cell: any unwanted scattering of the phenomenally intense x-ray beam by apparatus components such as windows, apertures, beam blocks, x-ray beamline components, or even passage through air, can easily overwhelm the weak scattering signals from the low-density target gas. Moreover, since the scattering signals change upon optical excitation by a mere 1%, any background signal could produce shot noise large enough to mask the pump–probe signals.

To address these challenges, we developed a windowless scattering cell where the low-pressure sample gas streams into a vacuum through a small orifice through which both the laser and the x-ray pulses enter. Here we define 'windowless' in terms of the upstream side of the cell, as it is important to ensure that the primary x-ray beam does not scatter onto the detector from sources other than the sample itself. Importantly, the cell is designed such that any x-rays scattered by the entrance aperture are blocked from directly hitting the detector. Similarly, x-rays scattered from propagation of the primary x-ray beam through air cannot reach the detector pixels.

In order to maximize the scattering signal, one wishes to maximize the sample pressure. However, large pressures of strongly absorbing samples cause attenuation of the laser, limiting the amount of sample. Consequently, a compromise must be struck as is discussed in more detail below. In our experiments using the x-ray fundamental, the sample region pressure was regulated to a constant 3–4 Torr ($\sim 10^{17}$ molecules cm^{-3}), which implies for the selected x-ray diameters and interaction lengths a total of $\sim 8 \times 10^{12}$ molecules in the interaction region. For the 3ω x-ray experiments, where 100 times fewer photons were available, we used sample pressures up to 40–50 Torr. The latter conditions were not used for pump–probe experiments.

2.2.1. Sample cell. The sample cell comprises two adjacent cylinders (10 mm × 19.2 mm radius, 8.3 mm × 3.2 mm radius) and permits scattering into 13°–70° scattering angles (figure 3). This corresponds to 1.0–4.8 $Å^{-1}$ with 8.3 keV photons and 2.3–11.7 $Å^{-1}$ with 20.1 keV photons. In practice, the signals at each end of the range are weak and their utility limited by noise, which is a function of the number of scatterers and thus path length of gas exposed at each angle.

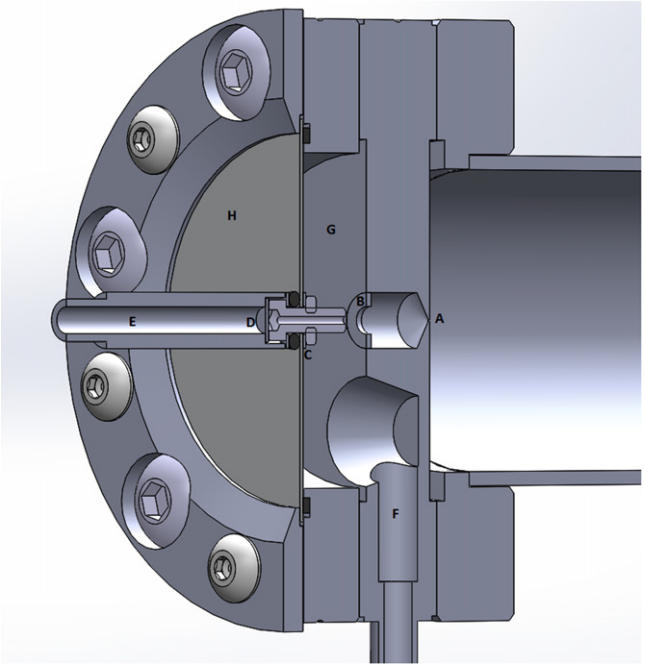

Figure 3. Close-up cross-section of the diffractometer. The x-rays enter the gas cell (G) from the vacuum side through a 200 μm aperture (A) and exit through a sapphire window (D), from where on they travel in air but are surrounded by lead shielding (E). Photons scattered from the aperture are blocked by the upper scatter limit (B) and the lower scatter limit (C), while photons scattered from the gas pass through the beryllium window (H).

2.2.2. Gas turnover. Because of the windowless design of the cell, there is a constant flow of gas. This has the advantage that, at any time, the sample probed in the cell does not contain a significant number of previously exposed molecules. The gas sample is continuously replenished by a feed line perpendicular to the incoming beams while the molecules in the sample region continuously escape into the upstream vacuum chamber through the 200 μm aperture. The resulting average distance traveled between pump–probe pairs in our experiment is thus found to be 2 mm. Since this is significantly larger than the width of the interaction region, which is 30 μm in diameter, the proportion of molecules probed multiple times in the experiment is negligible.

2.2.3. Scattering from apparatus components. Since gas-phase hydrocarbons are weak scatterers, it is vital to ensure that scattering of x-rays from the primary beam by any other source is eliminated. This also includes solid apparatus structures such as apertures and mirrors upstream of the diffractometer. The UV and x-ray photons are coupled into the diffractometer's sample region using a 200 μm aperture,

which separates the sample region from the vacuum-chamber that houses the in-coupling mirror. This aperture blocks transmission of x-rays scattered upstream of the in-coupling mirror and any residual gas, while permitting the transmission of the primary beam. Scattering of the primary x-ray beam by this aperture itself is blocked by a much larger-diameter aperture (upper scatter limit) within the sample region as well as by a beam-blocking washer (lower scatter limit) upstream from the beryllium window (figure 3). By judiciously selecting aperture sizes it is possible to largely prevent x-rays scattered from the 200 μm aperture from reaching the detector.

We note that x-rays scattered from the exit window, made from a thin piece of sapphire (figure 3), are prevented from reaching the detector by a lead shield. The same shield prevents x-rays scattered by air from reaching the detector. Finally we note that a 500 μm thick beryllium window (figure 3) is not in the path of the primary x-ray beam. While this window is traversed by x-rays scattered from the gas sample, the secondary scattering of those x-rays is negligible.

2.2.4. Focal parameters. In order to limit multi-photon processes that might place the molecule on highly excited surfaces or even ionize the molecules, the UV excitation laser was only weakly focused onto the sample such that it causes less than—but not much less than—10% excitation. Given the dual-aperture design described above, where the upstream region of the sample volume scatters onto low-q regions of the detector and the downstream region of the sample volume scatters onto high-q regions of the detector, the laser pulse may experience significant attenuation by the scattering molecules. To maintain the fraction of excited molecules along the length of probed molecules near 10%, we balanced the attenuation with the focal parameters of the excitation pulse.

The absorption of the UV pump beam follows the Beer–Lambert law, $\frac{I}{I_0} = 10^{-\sigma l N}$, where I_0 is the initial UV intensity, I is the intensity remaining after the beam propagates through the path length l, N is the number of scatterers in the path, and σ is the absorption cross section of the sample. Over the path length, strong absorbers significantly attenuate the intensity of the UV beam, which could result in a decreased fraction of excited scatterers toward the end of the path. To counteract this effect, the UV beam was focused at the downstream end of the sample cell, so that its beam diameter decreases as it traverses the sample cell. Fits of the theoretical calculations to the experimental data validated the results of this calculation.

2.3. Detection of scattered photons

The pattern of scattered x-ray photons is collected by a 2.3 megapixel Cornell-SLAC Pixel Array Detector (CSPAD) [49, 50] positioned approximately 4 cm from the scattering region. The scattering patterns were radially averaged to produce two-dimensional patterns, since the structural data is encoded in a nearly radially-symmetric signal. In order to interpret the results of the scattering experiments, a careful calibration of the instrumentation was necessary. Particularly important is the determination of the distance and the position of the CSPAD relative to the scattering cell.

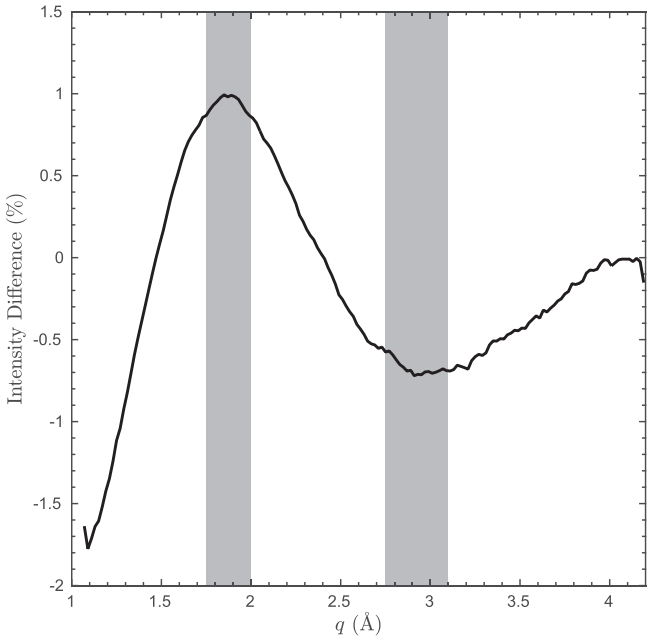

Figure 4. Experimental difference between pumped (+2 ps) and unpumped (−2 ps) CHD scattering patterns at 8.3 keV. Regions used to determine the center are highlighted.

2.3.1. Instrument calibration. Correction of gain differences between pixels, and calibration of the diffractometer geometry, were performed with scattering patterns collected from an atomic scatterer, Xenon. To determine a precise position of internal components, such as the vented screw and apertures, the difference between the collected and theoretical patterns was minimized. The Xenon pattern provides a correction factor, g, as a function of q,

$$g_{\mathrm{Xe}}(q) = \frac{I_{\mathrm{theoretical}}(q)}{I_{\mathrm{experimental}}(q)}. \quad (2)$$

In order to compare experimental to the theoretical scattering patterns, this factor was applied to all experimental scattering patterns.

2.3.2. Centering of the detector. Since the CSPAD is perpendicular to the primary x-ray beam, accurate radial and angular integrations of the scattering images requires calibration of the center of the image on the detector [51]. Since the transverse positional stability of the x-ray beam is better than 10 μm [31], a single determination of the center position is sufficient for all frames. To find the optimal Cartesian coordinates of the center of the image on the detector, the difference signal between pumped and unpumped 1,3-cyclohexadiene was examined and coordinates of the detector center were chosen that produce the largest intensity difference between the radial pattern's local maxima and local minima near 1.9 Å^{-1} and 3.0 Å^{-1}, respectively (figure 4). The difference pattern was smoothed to eliminate local minima due to noise. This was the only

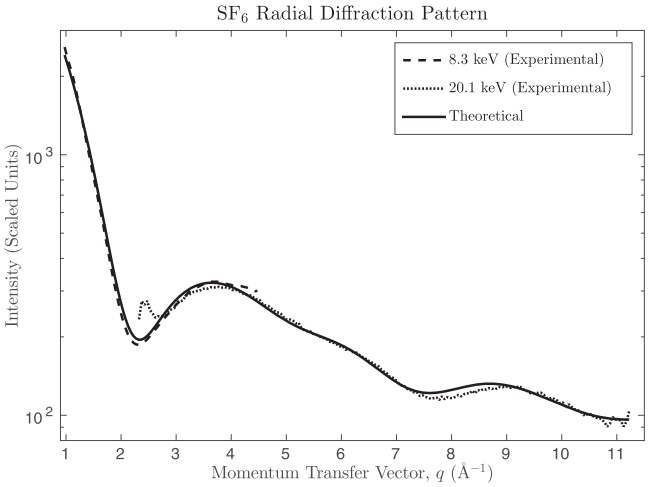

Figure 5. SF_6 scattering pattern with detector distance optimized for both 8.3 (fundamental) and 20.1 keV (3ω) experiments.

instance of data smoothing; no smoothed data was used for any purpose other than finding the detector center.

2.3.3. Calibration of detector distance. To ensure that the conversion from pixel coordinates to momentum transfer is properly performed, the distance between the diffractometer and the detector has to be determined. For this, sulfur hexafluoride (SF_6) was used as a model molecular scatterer, since its structure is well-known, including interatomic vibrational terms at room temperature [52], which modify the molecular scattering portion of equation (1) according to [53, 54]

$$I_{\mathrm{m}}(q) \propto \sum_{i\neq j}^{N_{\mathrm{atom}}} f_i(q) f_j(q) \exp\left(-\frac{1}{2} l_{\mathrm{m}}^2 q^2\right) \frac{\sin qr_{ij}}{qr_{ij}}, \qquad (3)$$

where l_{m}^2 is the mean vibrational amplitude of the associated interatomic distance.

The detector distance was found using a least-squares minimization of the percent difference between the radially-averaged theoretical and experimental patterns after the instrument function and center calibration corrections have been applied (figure 5). With this calibration, the detector distance was found to be 38.90 mm from the beryllium window in 8.3 keV experiments and 32.71 mm in 20.1 keV experiments, as shown in figure 5.

2.3.4. Photon counting. Raw images from the CSPAD are processed using a combination of techniques. First the dark image (also known as a 'pedestal'), collected during each data set, is subtracted on a per-pixel basis. Subsequently, the 'common mode' noise is removed from each tile individually using either of two techniques. In the first technique, used with 20.1 keV experiments, the mean value of all pixels with a value within 30 ADU above or below the pedestal is treated as the common mode noise value and subtracted from the value read from all other pixels on that tile. In the second technique, used with 8.3 keV experiments, the common mode value was calculated from a series of unbonded pixels on each ASIC, which experience common mode noise but are physically unable to provide a reading for the detection of a photon.

Because random and common-mode fluctuations over a large number of pixels risk dominating the number of photons scattered onto the detector, a hybrid photon-counting method was used wherein a lower limit was set for values to be recorded as non-zero. This number was set as 110 ADU for 20.1 keV photon experiments where the value for single photon detection was approximately 150 ADU. For the 8.3 keV photon experiments, when the value for a single photon was only 30 ADU, the lower threshold for photon counting was 2σ where the distribution of values in dark frames for each pixel was modeled as a Gaussian distribution. Above this threshold, the value of each pixel was retained (not converted into a number of photons) so that inter-pixel charge sharing of a single photon event would not be lost.

Several masking filters were applied to images to remove pixels that did not respond properly to photon absorption. In 20.1 keV experiments, pixels with extreme pedestal values (less than 1000 ADU or greater than 2000 ADU) were masked. This was only necessary for CSPAD version 1.3 and was therefore not used for 8.3 keV experiments, which were performed after CSPAD version 1.5 upgrades [55]. A mask was also made to ignore pixels with high photon counts, determined by the number of counts during vacuum-only exposures. These counts come from non-vapor sources and therefore the corresponding pixels are not suitable for lower-intensity gas scattering. Finally, a mask of 'dead' pixels, defined as pixels that never recorded photons during any exposure to gas samples of CHD, was applied.

Experiments using 20.1 keV x-ray photons also experienced larger gain differences (pixel-dependent responses in ADU per photon) because they also used the older, less consistent CSPAD version 1.3, so a gain map was made to normalize the single-photon peak of each pixel to 150 ADU using Xenon exposures. This was not necessary in 8.3 keV experiments, which used a more consistent CSPAD version 1.5.

2.4. Data treatment

Before the experimental scattering patterns are compared to theoretical patterns, the data is corrected for many effects unrelated to the molecular dynamics. These are discussed below.

2.4.1. Theoretical scattering patterns. In certain cases, it is necessary to produce absolute scattering patterns of gases, particularly of unreactive species such as xenon and sulfur hexafluoride. These heavier gases require more advanced modeling of their scattering intensities, because a dispersion correction has to be applied and the x-ray polarization has to be considered. Both terms are wavelength-dependent. The dispersion correction for forward scattering has both a real and an imaginary part, which transforms the atomic scattering

form factor to the form

$$f = f_0 + \Delta f' + i\Delta f''. \quad (4)$$

The necessary factors can be approximated from tabulated values at similar x-ray wavelengths [38, 56].

Because the x-ray source is horizontally polarized, photons are preferentially scattered in the vertical direction. Scattering images are corrected by a factor of $(\sin^2\varphi + \cos^2\varphi\cos^2 2\theta)$, where 2θ is the scattering angle and φ is the azimuthal angle as measured from the plane of polarization [57].

2.4.2. Difference scattering patterns. The changing scattering patterns in time-resolved experiments are best represented by difference patterns between the pattern of the ground-state molecule, derived either from patterns collected before time-zero or from frames where the UV pulse has been blocked, and the instantaneous scattering pattern, taken at a specific delay time after excitation. The difference patterns are particularly advantageous in cases where recording of an instrumental calibration with an atomic scatterer such as Xenon would be cumbersome, since they factor out a number of effects, including pixel-dependent gain differences. It is moreover convenient to express the difference pattern as a percentage

$$\%\Delta I(t, q, \gamma) = 100^* \frac{\Delta I(t, q, \gamma)}{I_{\text{off}}(q)}, \quad (5)$$

where γ is the fraction of excited molecules and $\Delta I(t, q, \gamma)$ is the *'laser on'-'laser off'* difference signal

$$\Delta I(t, q, \gamma) = I_{\text{on}}(t, q, \gamma) - I_{\text{off}}(q). \quad (6)$$

In using percentage differences, many signal contributions that do not change upon UV excitation cancel out, such as the magnitude of scattering intensity as a function of q (a result of the diffractometer's internal shape) and the atomic scattering signal. This results in scattering patterns that are independent of many experimental complications, and emphasizes the changing molecular scattering signal by eliminating the unchanging atomic scattering. Additionally, this representation improves the visualization of pattern elements at large q-values, where absolute differences would show only small changes.

2.4.3. Data acquisition. Datasets were collected in runs of approximately 1000 frames per time point, including frames with neither x-ray nor UV laser exposure ('dark'), frames with x-ray exposure only, and frames with both UV and x-ray exposure. To ensure consistency in x-ray performance, frames were collected in a 17:17:1 ratio of UV-on: UV-off: dark frames while time points were collected in randomized order, minimizing the effect of systematic drifts in x-ray or UV performance.

2.4.4. Scaling. Since the number of x-ray photons per pulse can vary up to 100% shot-to-shot [25], the scattering patterns have to be carefully scaled. The most accurate method found to determine the relative number of photons in each shot is to integrate the number of photons collected by the detector. Consequently, the scattering patterns were scaled by the detector's total integrated intensity after radial averaging. Although one might expect that time-evolving structures might exhibit different sums in the observed scattering region, the low percentage of excited molecules suggests that this fluctuation is minimal. Moreover, for our data analysis we used the same scaling method in computing the expected theoretical patterns, so that any such errors should have no impact on the derived molecular structures.

2.4.5. Attenuation. Since the scattered x-ray photons travel through several components prior to the detector, the images are adjusted to account for attenuation by these materials.

In all scattering patterns, beryllium is the largest but most consistent attenuator of scattered photons. At a thickness of 500 μm, this window transmits 91.8% of 8.3 keV photons and 98.3% of 20.1 keV photons [58]. However, since the scattered photons do not traverse the window perpendicularly, photons scattered to large q-values experience a longer path length through beryllium (up to 1366 μm). Consequently, a q-dependent scaling factor has to be applied to the scattering intensity. A similar factor has to be applied to account for the attenuation by the air between the scattering cell and the detector. The attenuation by air at standard conditions for the relevant path lengths (between 4 and 12 cm) is 4.0%–11.6% for 8.3 keV x-rays and 0.3%–1.0 % for 20.1 keV x-rays [58].

Within the chamber itself, the attenuation depends on the sample gas, through which scattered x-ray photons traverse up to 22.5 mm. This gives a significant effect in Xenon, where the 8.3 keV x-rays are attenuated by up to 4.5% at 10 Torr and 293 K, whereas the 20.1 keV photons are only attenuated by up to 0.4% under the same conditions. In SF_6 the effect is small, with attenuations of up to 2.3% for 8.3 keV photons at 45 Torr and 293 K but only up to 0.17% of 20.1 keV photons [58]. The attenuation of scattered x-ray photons by 1,3-cyclohexadiene was negligible at the pressure of our studies, 3–4 Torr [58].

2.4.6. Detector planarity. To eliminate another source of instrument-specific effects on the scattering patterns, the scattering angle dependence of the distance of the detector from the sample cell is accounted for. The scattering intensity decays as $\frac{1}{R^2}$, where R is the distance between the scattering center and the detector. In the far-field limit this factor is uniform for every point on the detector. However, in our experiment, where the detector is less than 40 mm from the sample cell, R ranges from 60 to 120 mm. To account for this, the recorded intensity after radial integration is multiplied by R^2 to normalize intensities across the detector.

Similarly, the scattering patterns were corrected to replace the nominal pixel size (110 μm × 110 μm) with an 'effective' pixel size, defined as the projection of the pixel area normal to the scattering center for that pixel.

2.4.7. Matching theoretical predictions to experimental observation. In order to analyze the scattering data, we use

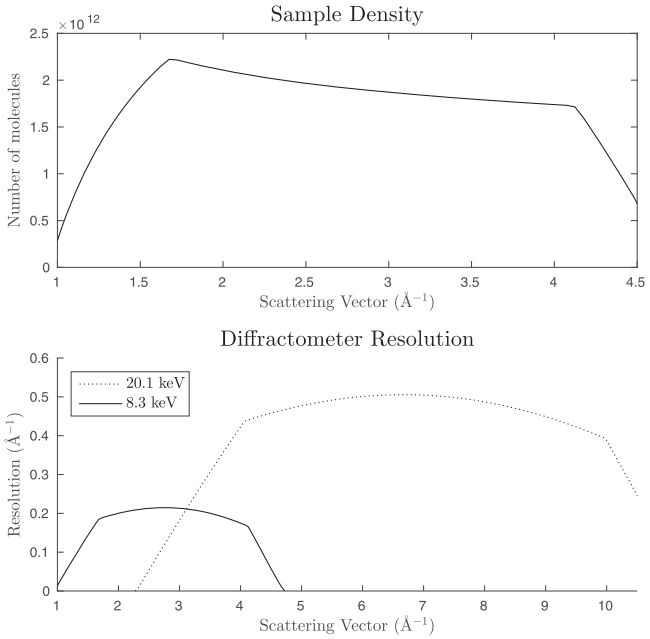

Figure 6. (Top) Number of gas molecules exposed to each position on the detector at 3.7 Torr for 8.3 keV photons. (Bottom) Experimental resolution at 8.3 and 20.1 keV x-ray, limited by the difference between maximum and minimum scattering vector visible to each nominal scattering vector.

an optimization procedure to match theoretically predicted scattering patterns to the observed time-resolved signal. Inversion procedures that yield nuclear density distributions exist for diatomic [59, 60] and polyatomic [60, 61] molecules, but the limited q-range in the present measurements render these approaches infeasible. Instead, we use state-of-the-art *ab initio* nonadiabatic quantum molecular dynamics simulations [43, 44] to restrict the available configuration space in an accurate manner. A large number of trajectories, each representing a feasible reaction path for the CHD ring-opening reaction, are used to fit the observed experimental signal

$$I(t, q) = \sum_k w_k^2 I_k(t, q), \tag{7}$$

where $I(t, q)$ is the predicted signal, w_k^2 are the weights for the ensemble of trajectories, with $\sum_k w_k^2 = 1$, and $I_k(t, q)$ is the scattering signal for each trajectory, calculated using the Debye formula in equation (1) with additional corrections for inelastic scattering. The approximations inherent in this approach, and further details regarding the simulations and the optimization procedure, are discussed elsewhere [43, 44, 62, 63]. We focus here on how the signal in equation (7) is processed for comparison to the experimental signal. As seen in section 2.4.2, the experimental signal is represented by a percentage '*laser on*'-'*laser off*' signal. If the '*laser on*' signal is

$$I_{\text{on}}(t, q, \gamma) = \gamma I_{\text{exc}}(t, q) + (1 - \gamma) I_{\text{off}}(q), \tag{8}$$

where γ is the excitation fraction, $I_{\text{exc}}(t, q)$ the signal from the excited molecules, and $I_{\text{off}}(q)$ is the '*laser off*' signal, then the difference signal becomes $\Delta I(t, q, \gamma) = \gamma(I_{\text{exc}}(t, q) - I_{\text{off}}(q))$. However, this expression is only valid if the x-ray pulse intensity is the same for both the '*on*' and the '*off*' signals. In the XFEL measurements, the intensity of the x-ray pulses fluctuates significantly, and we therefore scale the '*on*' signal with respect to the total detected intensity of the '*off*' signal

$$\Delta I(t, q, \gamma) = \frac{Q_{\text{off}}}{Q_{\text{on}}(t, \gamma)} I_{\text{on}}(t, q, \gamma) - I_{\text{off}}(q), \tag{9}$$

where Q_{off} is the integrated intensity on the detector for the '*off*' signal, and $Q_{\text{on}}(t, \gamma)$ is the integrated intensity for the '*on*' signal. It is straightforward to modify the difference signal in equation (9) to account for q-dependent excitation fraction, in the case of a long interaction region in the experiment. Finally, since the experimental signal tapers off for larger values of q, it is better to use a percentage difference signal

$$\%\Delta I(t, q, \gamma) = 100 \times \frac{\Delta I(t, q, \gamma)}{I_{\text{off}}(q)}. \tag{10}$$

The predicted signal must also be convoluted to match the duration of the pump and probe pulses, and, finally, the theoretical signal is time-shifted relative the experimental signal to optimize the fit to the experiment. The optimization procedure therefore scans the trajectory weights, w_k^2, the excitation fraction γ, and the exact time zero within the experimental limits.

3. Results and discussion

The low signal level associated with gas-phase x-ray scattering experiments was overcome by higher pressure, longer path length, and use of the hybrid photon counting method. Careful consideration and implementation of all these techniques has made it possible to produce high quality scattering patterns with a very small number of scattering molecules. With a long column of reacting molecules, loss of resolution arises from the number of different scattering angles visible to each point on the detector. The upper and lower scatter limits reduce this loss of resolution, however, by limiting the length of gas exposed that is visible to each pixel. Although the overall length of scattering gas is 13.5 mm, in this double-aperture design only 5–6 mm is visible to any point on the detector, giving a resolution of around 0.25 Å^{-1} and 0.50 Å^{-1} over all regions for 8.3 keV and 20.1 keV x-ray photons respectively (figure 6). To ensure that this does not introduce errors into the theoretically-fit models, simulated scattering patterns are convoluted by the range of scattering vector visible to each nominal q value.

After radial averaging, the scattering patterns are corrected by the number of visible scatterers as a function of scattering vector, q. At 3.7 Torr, the majority of the detector is exposed to 2×10^{-12} molecules (figure 6).

The use of two separate laser systems for the pump- and probe-pulses produced some variability in their co-timing. Beyond the determination of time-zero, high time resolution was achieved through the use of a spectral time-tool [48].

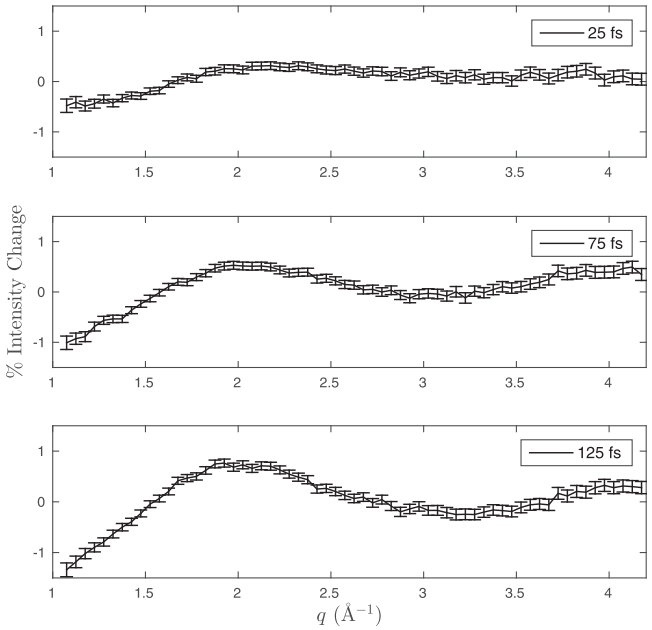

Figure 7. Experimental CHD results at 25, 75, and 125 fs. Error bars are shown to three sigma, calculated from the shot noise of the CSPAD detector.

Shown in figure 2 are the time-delays determined for four sets of nominal (intended) time points, showing that data can be collected with a time resolution that exceeds the jitter of the LCLS source. The background scattering levels were minimized by the use of apertures, which were designed such that scattering of the primary x-ray beam by any source upstream of the sample gas would be attenuated by a thick metallic surface and scattering from any source downstream of the sample gas would be attenuated by a lead foil positioned prior to the detector (figure 3). The result of this was very low-noise CHD diffraction patterns, as shown in figure 7.

4. Summary

We demonstrated a windowless cell diffractometer for ultrafast gas phase x-ray scattering experiments that can be used for a range of hard x-ray wavelengths. This diffractometer offers several benefits over molecular beams or nozzle setups, including a higher number of scatterers (to overcome the low scattering cross-section of small hydrocarbons) and the necessary apertures to prevent upstream scattering from reaching the detector.

This experimental design has been demonstrated to provide adequate scattering patterns for low-pressure gases with sufficient resolution to perform time-resolved dynamical studies, and is intended to work for a large number of molecular systems. It has successfully generated patterns for 1,3-cyclohexadiene, sulfur hexafluoride, and xenon at pressures ranging from 3 to 50 Torr, and we anticipate this design to be useful for a number of other molecules in future studies.

Future studies will utilize a simplified diffractometer geometry wherein the sample cell will exhibit a reduced reaction path length, thereby relaxing the high focusing parameter requirements of a long path. The simplification of the diffractometer may also permit scattering at much larger angles and therefore obtain a wider range of q, increasing the experimental resolution and possibly eliminating the technique's substantial reliance on sophisticated quantum calculations. Such experiments would be possible in the CXI hutch at LCLS. Future experiments could also improve the spatial resolution of the molecular target by employing molecular alignment techniques.

Acknowledgments

Use of the Linac Coherent Light Source (LCLS), SLAC National Accelerator Laboratory, is supported by the US Department of Energy, Office of Science, Office of Basic Energy Sciences under Contract No. DE-AC02-76SF00515. The project benefited also from funding by the National Science Foundation, Grant No. CBET-1336105. Computational work (AK) was supported by grants FP7-PEOPLE-2013-CIG-NEWLIGT from the European Union and RPG-2013-365 from the Leverhulme Trust.

References

[1] Zewail A H 2000 Femtochemistry: atomic-scale dynamics of the chemical bond *J. Phys. Chem.* A **104** 5660–94
[2] Eigen M 1971 Selforganization of matter and the evolution of biological macromolecules *Naturwissenschaften* **58** 465–523
[3] Zewail A H 1996 Femtochemistry: recent progress in studies of dynamics and control of reactions and their transition states *J. Phys. Chem.* **100** 12701–24
[4] Schultz T, Quenneville J, Levine B, Toniolo A, Martínez T J, Lochbrunner S, Schmitt M, Shaffer J P, Zgierski M Z and Stolow A 2003 Mechanism and dynamics of azobenzene photoisomerization *J. Am. Chem. Soc.* **125** 8098–9
[5] Hockett P, Bisgaard C Z, Clarkin O J and Stolow A 2011 Time-resolved imaging of purely valence-electron dynamics during a chemical reaction *Nat. Phys.* **7** 612–5
[6] Felker P M and Zewail A H 1983 Observation of restricted IVR in large molecules: quasi-periodic behavior, phase-shifted and non-phase-shifted quantum beats *Chem. Phys. Lett.* **102** 113–9
[7] Dantus M, Rosker M J and Zewail A H 1988 Femtosecond real-time probing of reactions: II. The dissociation reaction of ICN *J. Chem. Phys.* **89** 6128
[8] Gosselin J L, Minitti M P, Rudakov F M, Sølling T I and Weber P M 2006 Energy flow and fragmentation dynamics of N,N-Dimethylisopropylamine *J. Phys. Chem.* A **110** 4251–5
[9] Minitti M P, Zhang Y, Rosenberg M, Brogaard R Y, Deb S, Sølling T I and Weber P M 2012 Far-UV photochemical bond cleavage of n-amyl nitrite: bypassing a repulsive surface *J. Phys. Chem.* A **116** 810–9
[10] Pemberton C C, Zhang Y, Saita K, Kirrander A and Weber P M 2015 From the (1B) spectroscopic state to the photochemical product of the ultrafast ring-opening of 1,3-cyclohexadiene: a spectral observation of the complete reaction path *J. Phys. Chem.* A **119** 8832–45

[11] Cheng X, Zhang Y, Gao Y, Jónsson H and Weber P M 2015 Ultrafast STRUCTURAL PATHWAY OF CHARGE TRANSFER in N,N,N′,N′-tetramethylethylenediamine *J. Phys. Chem.* A **119** 2813–8
[12] Cheng X, Zhang Y, Deb S, Minitti M P, Gao Y, Jónsson H and Weber P M 2014 Ultrafast structural dynamics in Rydberg excited N,N,N′,N′-tetramethylethylenediamine: conformation dependent electron lone pair interaction and charge delocalization *Chem. Sci.* **5** 4394–403
[13] Gessner O *et al* 2006 Femtosecond multidimensional imaging of a molecular dissociation *Science* **311** 219–22
[14] Bisgaard C Z, Clarkin O J, Wu G, Lee A M D, Gessner O, Hayden C C and Stolow A 2009 Time-resolved molecular frame dynamics of fixed-in-space CS2 molecules *Science* **323** 1464–8
[15] Ihee H, Lorenc M, Kim T K, Kong Q Y, Cammarata M, Lee J H, Bratos S and Wulff M 2005 Ultrafast x-ray diffraction of transient molecular structures in solution *Science* **309** 1223–7
[16] Siwick B J, Dwyer J R, Jordan R E and Miller R J D 2003 An atomic-level view of melting using femtosecond electron diffraction *Science* **302** 1382–5
[17] Siwick B J, Dwyer J R, Jordan R E and Miller R J D 2004 Femtosecond electron diffraction studies of strongly driven structural phase transitions *Chem. Phys.* **299** 285–305
[18] Harb M, Ernstorfer R, Hebeisen C T, Sciaini G, Peng W, Dartigalongue T, Eriksson M a., Lagally M G, Kruglik S G and Miller R J D 2008 Electronically driven structure changes of si captured by femtosecond electron diffraction *Phys. Rev. Lett.* **100** 155504
[19] Hada M, Pichugin K and Sciaini G 2013 Ultrafast structural dynamics with table top femtosecond hard x-ray and electron diffraction setups *Eur. Phys. J. Spec. Top.* **222** 1093–123
[20] Hastings J B, Rudakov F M, Dowell D H, Schmerge J F, Cardoza J D, Castro J M, Gierman S M, Loos H and Weber P M 2006 Ultrafast time-resolved electron diffraction with megavolt electron beams *Appl. Phys. Lett.* **89** 184109
[21] van Oudheusden T, Pasmans P L E M, van der Geer S B, de Loos M J, van der Wiel M J and Luiten O J 2010 Compression of subrelativistic space-charge-dominated electron bunches for single-shot femtosecond electron diffraction *Phys. Rev. Lett.* **105** 264801
[22] Weathersby S P *et al* 2015 Mega-electron-volt ultrafast electron diffraction at SLAC national accelerator laboratory *Rev. Sci. Instrum.* **86** 073702
[23] Siwick B J, Dwyer J R, Jordan R E and Miller R J D 2002 Ultrafast electron optics: propagation dynamics of femtosecond electron packets *J. Appl. Phys.* **92** 1643
[24] Aidelsburger M, Kirchner F O, Krausz F and Baum P 2010 Single-electron pulses for ultrafast diffraction *Proc. Natl Acad. Sci. USA* **107** 19714–9
[25] Ernstorfer R, Harb M, Hebeisen C T, Sciaini G, Dartigalongue T and Miller R J D 2009 The formation of warm dense matter: experimental evidence for electronic bond hardening in gold *Science* **323** 1033–7
[26] Jean-Ruel H, Gao M, Kochman M a., Lu C, Liu L C, Cooney R R, Morrison C A and Miller R J D 2013 Ring-closing reaction in diarylethene captured by femtosecond electron crystallography *J. Phys. Chem.* B **117** 15894–902
[27] Ihee H, Lobastov V A, Gomez U M, Goodson B M, Srinivasan R, Ruan C Y and Zewail A H 2001 Direct imaging of transient molecular structures with ultrafast diffraction *Science* **291** 458–62
[28] Dudek R C and Weber P M 2001 Ultrafast diffraction imaging of the electrocyclic ring-opening reaction of 1,3-Cyclohexadiene *J. Phys. Chem.* A **105** 4167–71
[29] Minitti M P *et al* 2015 Optical laser systems at the linac coherent light source *J. Synchrotron Radiat.* **22** 526–31
[30] Berger M J, Hubbell J H, Seltzer S M, Chang J, Coursey J S, Sukumar R, Zucker D S and Olsen K 1998 XCOM: photon cross sections database *NIST Standard Reference Database 8 (XGAM)* NBSIR 87-3597 (www.nist.gov/pml/data/xcom)
[31] Emma P *et al* 2010 First lasing and operation of an ångstrom-wavelength free-electron laser *Nat. Photonics* **4** 641–7
[32] Seibert M M *et al* 2011 Single mimivirus particles intercepted and imaged with an x-ray laser *Nature* **470** 78–81
[33] Chapman H N *et al* 201 Femtosecond x-ray protein nanocrystallography *Nature* **470** 73–7
[34] Barends T R M *et al* 2014 *De novo* protein crystal structure determination from x-ray free-electron laser data *Nature* **505** 244–7
[35] Kang Y *et al* 2015 Crystal structure of rhodopsin bound to arrestin by femtosecond x-ray laser *Nature* **523** 561–7
[36] McFarland B K *et al* 2014 Ultrafast x-ray Auger probing of photoexcited molecular dynamics *Nat. Commun.* **5** 4235
[37] Debye P 1915 Zerstreuung von röntgenstrahlen *Ann. Phys.* **351** 809–23
[38] Wilson A 1995 *International Tables for Crystallography, Vol. C, Mathematical, physical, and Chemical Tables* (Dordrecht: Kluwer)
[39] Reckenthaeler P, Centurion M, Fuß W, Trushin S A, Krausz F and Fill E E 2009 Time-resolved electron diffraction from selectively aligned molecules *Phys. Rev. Lett.* **102** 213001
[40] Ryu S, Weber P M and Stratt R M 2000 The diffraction signatures of individual vibrational modes in polyatomic molecules *J. Chem. Phys.* **112** 1260
[41] Garavelli M, Page C S, Celani P, Olivucci M, Schmid W E, Trushin S A and Fuss W 2001 Reaction path of a sub-200 fs photochemical electrocyclic reaction *J. Phys. Chem.* A **105** 4458–69
[42] Deb S and Weber P M 2011 The ultrafast pathway of photon-induced electrocyclic ring-opening reactions: the case of 1,3-cyclohexadiene *Annu. Rev. Phys. Chem.* **62** 19–39
[43] Minitti M P *et al* 2014 Toward structural femtosecond chemical dynamics: imaging chemistry in space and time *Faraday Discuss.* **171** 81–91
[44] Minitti M P *et al* 2015 Imaging molecular motion: femtosecond x-ray scattering of an electrocyclic chemical reaction *Phys. Rev. Lett.* **114** 255501
[45] Chollet M *et al* 2015 The x-ray pump–probe instrument at the linac coherent light source *J. Synchrotron Radiat.* **22** 503–7
[46] Fritz D M *et al* 2007 Ultrafast bond softening in bismuth: mapping a solid's interatomic potential with x-rays *Science* **315** 633–6
[47] Wilcox R, Byrd J M, Doolittle L, Huang G and Staples J W 2009 Stable transmission of radio frequency signals on fiber links using interferometric delay sensing *Opt. Lett.* **34** 3050–2
[48] Bionta M R *et al* 2014 Spectral encoding method for measuring the relative arrival time between x-ray/optical pulses *Rev. Sci. Instrum.* **85** 083116
[49] Philipp H T, Hromalik M, Tate M, Koerner L and Gruner S M 2011 Pixel array detector for x-ray free electron laser experiments *Nucl. Instrum. Methods Phys. Res.* **649** 67–9
[50] Blaj G *et al* 2015 X-ray detectors at the linac coherent light source *J. Synchrotron Radiat.* **22** 577–83
[51] Cardoza J D, Hromalik M, Tate M, Koerner L and Gruner S M 2011 Pixel array detector for x-ray free electron laser experiments *Nucl. Instrum. Methods Phys. Res.* **649** 67–9
[52] Miller B R and Fink M 1981 Mean amplitudes of vibration of SF6 and intramolecular multiple scattering *J. Chem. Phys.* **75** 5326–8
[53] Hargittai I 1988 Stereochemical applications of gas-phase electron diffraction *Stereochemical Applications of Gas-Phase Electron Diffraction* ed I Hargittai and M Hargittai (New York: Wiley) pp 55–84

[54] Ruan C Y, Lobastov V A, Srinivasan R, Goodson B M, Ihee H and Zewail A H 2001 Ultrafast diffraction and structural dynamics: the nature of complex molecules far from equilibrium *Proc. Natl Acad. Sci. USA* **98** 7117–22
[55] Herrmann S *et al* 2014 CSPAD upgrades and CSPAD V1.5 at LCLS *J. Phys.: Conf. Ser.* **493** 012013
[56] Henke B L, Gullikson E M and Davis J C 1993 X-ray interactions: photoabsorption, scattering, transmission, and reflection at $E = 50$–$30\,000$ eV, $Z = 1$–92 *At. Data Nucl. Data Tables* **54** 181–342
[57] Warren B E 1990 *X-ray Diffraction* (Mineola, New York: Dover)
[58] Gullikson E 1995 *X-ray Interactions with Matter* (http://henke.lbl.gov/optical_constants/)
[59] Cao J and Wilson K R 1998 Ultrafast x-ray diffraction theory *J. Phys. Chem.* A **102** 9523–30
[60] Lorenz U, Møller K B and Henriksen N E 2010 Theory of time-resolved inelastic x-ray diffraction *Phys. Rev.* A **81** 023422
[61] Srinivasan R, Lobastov V A, Ruan C-Y and Zewail A H 2003 Ultrafast electron diffraction (UED) *Helv. Chim. Acta* **86** 1761–99
[62] Vendrell O *et al* 2014 Chemical reaction dynamics I and electron dynamics in molecules: general discussion *Faraday Discuss.* **171** 145–68
[63] Kirrander A, Saita K, Budarz J M, Minitti M P and Weber P M 2016 in preparation